




PAPER

Cite this: *Nanoscale Adv.*, 2024, 6, 4693

A field-portable electrochemical immunosensor based on a multifunctional $\text{Ag}_2\text{O}/\text{g}-\text{C}_3\text{N}_4@\text{MA-DBB}$ covalent organic framework receptor interface for single-step detection of aflatoxin M_1 in raw milk samples†

Iram Naz, ^{ab} Akhtar Hayat, ^{*b} Farhat Jubeen, ^{*a} Sadia Asim^a and Abida Kausar^a

Aflatoxin M_1 (AFM_1), a hydroxylated metabolite of aflatoxin B_1 (AFB_1), contaminates milk and dairy products from livestock *via* ingestion of feed contaminated with a species of *Aspergillus*. As AFM_1 is a Group-II B carcinogen, it is indispensable to develop novel, easy-to-handle, sensitive, portable and cost-effective strategies for its detection. Herein, a covalent organic framework (COF)-based electroactive nanocomposite, $\text{Ag}_2\text{O}/\text{g}-\text{C}_3\text{N}_4-\text{COOH}@\text{MA-DBB-COF}$ (silver oxide/carboxy-functionalized graphitic carbon nitride@melamine-dibromo butane COF), is designed to serve as a multifunctional receptor surface. The $\text{Ag}_2\text{O}/\text{g}-\text{C}_3\text{N}_4-\text{COOH}@\text{MA-DBB-COF}$ formation was characterized through X-ray diffraction (XRD), Fourier transform infrared (FTIR) spectroscopy, micro-Raman spectroscopy (RAMAN), dynamic light scattering (DLS) and thermogravimetric analysis (TGA), and each step of the sensor fabrication was monitored using field emission scanning electron microscopy (FE-SEM), cyclic voltammetry (CV) and electrochemical impedance spectroscopy (EIS). Under the optimal conditions, the designed immunosensor permitted the detection of AFM_1 in the linear range of 0.03–1000 fg mL^{-1} , with a 0.01 fg mL^{-1} limit of detection (LOD). The selectivity of the designed immunosensor was validated *via* an anti-interference study. The practical applicability of the immunosensor was demonstrated by the detection of AFM_1 in real milk samples, and good recovery values (97.28–102.62%) were obtained. Furthermore, the developed immunosensor and high-performance liquid chromatography (HPLC) were employed in parallel to detect AFM_1 in local market milk samples from twenty different sites to validate the performance of the newly designed immunosensor. Additionally, the designed immunosensor was stable over an extended period of time. This work reports a single-step field-portable multifunctional innovative electrochemical immunoreceptor design for on-site and label-free detection of AFM_1 in milk samples. Hence, the present study is the first report on the fabrication of a multifunctional innovative electrochemical immunoreceptor based on $\text{PGE}/\text{Ag}_2\text{O}/\text{g}-\text{C}_3\text{N}_4-\text{COOH}@\text{MA-DBB-COF}$ for the detection of AFM_1 in milk samples.

Received 19th April 2024
Accepted 12th July 2024

DOI: 10.1039/d4na00327f

rsc.li/nanoscale-advances

1. Introduction

Milk is an essential dietary element that is rich in micro- and macronutrients. It plays a vital role in growth and development, especially in infants and children.^{1,2} The quality of milk is deteriorated by contaminants such as aflatoxins, particularly AFM_1 .³ Aflatoxins are structurally related toxic secondary

metabolites produced by species of *Aspergillus* in corn, rice, nuts, peanuts, coconut, dried fruits and spices.^{4–8} Among the more than 20 different aflatoxins, AFB_1 is the most toxic.⁹ AFM_1 is a hydroxylated metabolite of AFB_1 .¹⁰ AFB_1 from contaminated animal feed is metabolized in the liver by cytochrome P-450 to AFM_1 and excreted in the milk directly, contaminating milk and dairy products.¹¹ Its toxicity profile includes growth retardation, immunosuppression, genotoxicity, and carcinogenicity.^{12,13} AFM_1 was initially classified as a group IIB human carcinogen by IARC and has recently been moved to group I.¹⁴ Due to its extreme toxicity, maximum permissible limits for AFM_1 in milk ranging from 0.025 to 0.5 $\mu\text{g L}^{-1}$ have been set by food regulatory agencies such as FAO and EC.¹⁵

AFM_1 is highly thermostable and resistant to conventional cooking and food processing practices such as irradiation,

^aDepartment of Chemistry, Govt College Women University, Arfa Kareem Road, Faisalabad, 38000, Pakistan. E-mail: dr.farhatjubeen@gcwuf.edu.pk

^bInterdisciplinary Research Center in Biomedical Materials (IRCBM), COMSATS University Islamabad, Lahore Campus, 1.5 km Defense Road, Off Raiwind Road, Lahore 54000, Punjab, Pakistan. E-mail: akhtarhayat@cuilahore.edu.pk

† Electronic supplementary information (ESI) available. See DOI: <https://doi.org/10.1039/d4na00327f>



pasteurization, and ultraheat treatment (UHT). Prolonged exposure to AFM₁ is very dangerous, even at low concentrations.¹⁶ In order to maintain food safety and human health, accurate monitoring of AFM₁ is of fundamental importance. The established methods for the detection of AFM₁ include thin layer chromatography (TLC) modified to high performance HPTLC, high-performance liquid chromatography-fluorescence detection (HPLC-FLD), liquid chromatography coupled tandem mass spectrometry (LC-MS/MS) and enzyme-linked immunosorbent assay (ELISA).^{17–20} Although chromatographic techniques are accurate, promising high sensitivity, they require tedious and costly sample clean-up procedures, highly expensive and massive equipment, and skilled personnel to attain good accuracy and precision.²¹ The downsides of ELISA are extended incubation times, frequent inaccurate positive or negative screening reports, less sensitivity and inadequate detection range.^{22,23} Hence, it is indispensable to develop novel, easy-to-handle, sensitive, portable, compact-sized and cost-effective strategies for AFM₁ detection.

With the advent of nanotechnology, currently, immunosensors with improved sensitivity and selectivity represent an attractive field of analytical research for aflatoxin detection.²⁴ A number of AFM₁ immunosensors have been reported using discrete nanoparticles (NPs) such as Au NPs, quantum dots, Fe₂O₃ NPs, Ni NPs, Fe₃O₄ NPs, and countless others to perform one particular function to improve the analytical figure of merit.^{25–29} Recently, using ELISA with N-doped photoluminescent carbon dots, ultrasensitive detection of AFM₁ was achieved with a high quantum yield.³⁰ Further, a strong anti-idiotypic nanobody was used on a screen-printed carbon electrode to replace a highly toxic synthetic antibody for quantitative AFM₁ detection through chronoamperometry.³¹ However, multiphase nanocomposite materials prepared by combining two or more different constituents in one material can perform multifunctional roles. Each constituent offers exceptional tunable properties due to its small size, large surface-to-volume ratio, and, particularly, due to the interfacial interaction among the phases.^{32,33} An immunosensor for robust AFM₁ detection was designed using graphene oxide-chitosan and cerium oxide-chitosan on a screen-printed electrode.³⁴ A nanocomposite consisting of metal-organic-framework-incorporated dichalcogenide quantum dots was fabricated on a screen-printed electrode for the monitoring of AFM₁.³⁵ Herein, the synthesis of a novel COF-based multifunctional nanocomposite material is reported to improve the analytical performance of a single-step-operation immunosensor for the ultrasensitive detection of AFM₁ in milk samples.

The application of graphitic carbon nitride (g-C₃N₄) in analytical disciplines is attributed to its exceptional surface properties such as biocompatibility, ease of surface functionalization and hydrogen bonding.^{36,37} Moreover, its restricted electrochemical performance due to its chemical inertness and poor conductivity^{38,39} has been improved by customization with nanomaterials.^{40–43} The present study reports the design and fabrication of a novel electrochemical immunosensor based on a binary metal oxide (Ag₂O) incorporated in g-C₃N₄ and modified with a porous crystalline polymer matrix. Nanomaterials

are frequently modified by means of direct functionalization during synthesis or coating with functional polymers without affecting their specific properties.⁴⁴ Such functionalization not only allows reproducible immobilization of bioreceptor units, but can also increase the biocompatibility of these materials.⁴⁵ In the present study, Ag₂O/g-C₃N₄ was acidified to Ag₂O/g-C₃N₄-COOH to offer a covalent immobilization site for the probe as well as signal magnification to develop a label-free electrochemical sensor.

The tunable properties of COFs, such as their high surface area, variable porosity, thermal and chemical stability, and high electrical conductivity, has made them materials of choice for diverse applications.⁴⁶ In the present study, a melamine- and 1,4-dibromobutane-based synthesized MA-DBB-COF was ligated with Ag₂O/g-C₃N₄-COOH through van der Waals interactions. This developed *via* the lone pairs available at the N of g-C₃N₄ and -N-H of the COF and was conducive for charge transfer. Hence, the incorporation of MA-DBB-COF improved the electrical conductivity of the immunosensor, leading to further signal amplification. In the designed nanocomposite, the Ag in Ag₂O served as a signal-generating probe to produce a precise electric readout of the presence of the analyte with high sensitivity. g-C₃N₄-COOH, which exhibits high biocompatibility, served as a covalent immobilization site for the probe and bio-recognition unit. g-C₃N₄-COOH can develop an amide linkage with the amino group of bio-receptors or can be functionalized as g-C₃N₄-NH₂ to develop a similar linkage with the -COOH group of the bioreceptors. Thus, functionalized g-C₃N₄ offers wide-scale biocompatibility as an immobilization support. The ability of the nanocomposite material to be electrochemically oxidized is the basis of the sensing of the analyte by generating a direct oxidation read-out signal. Thus, the intrinsic oxidation signal of the synthesized nanocomposite served not only as an analytical signal, but also as a label to detect the analyte. The designed hybrid nanocomposite material offers: (i) automated signal generation, (ii) immobilization of the probe and bioreceptor on the transducer platform, and (iii) synergistic conductivity for signal amplification. The designed nanocomposite material is applied on a pencil graphite electrode (PGE) to fabricate the immunosensor for the detection of AFM₁. To the best of our knowledge, the present study is the first report on the fabrication of a multifunctional innovative electrochemical immunoreceptor based on PGE/Ag₂O/g-C₃N₄-COOH@MA-DBB-COF for AFM₁ detection in milk samples.

2. Methodology

2.1. Chemicals & apparatus

All the reagents used in the experimental section were of analytical grade. Melamine (C₃N₃(NH₂)₃) (Dae-Jung), 1,4-dibromobutane (C₄H₈Br₂), dimethyl sulfoxide (C₂H₆OS), sodium hydroxide (NaOH), *N*-hydroxy succinimide (C₄H₅NO₃) (NHS), *N*-(3-dimethylaminopropyl)-*N'*-ethyl-carbodiimide hydrochloride (C₈H₁₇N₃) (EDC), AFM₁ (C₁₇H₁₂O₇) and anti-AFM₁ monoclonal antibody were purchased from Alfa Aesar. Chloroacetic acid (C₂H₃ClO₂), potassium ferricyanide (K₃Fe(CN)₆), potassium

ferrocyanide ($K_4Fe(CN)_6$), and phosphate buffer saline tablets ($Cl_2H_3K_2Na_3O_8P_2$) pH 7.4 were purchased from UNI-CHEM. Bovine serum albumin (BSA, MW 66 kDa) was from Sigma Aldrich, France. All solutions were prepared in distilled water.

An electrochemical workstation (Potentiostat Interface GAMRY 1010E, USA), equipped with a platinum counter electrode, Ag/AgCl as a reference electrode and PGE as the working electrode was used for electrochemical measurements. The immunosensor was designed as PGE/Ag₂O-g-C₃N₄-COOH@MA-DBB-COF. The surface morphology of the gradual fabrication of PGE was studied using FE-SEM (Apreo S, Thermo Fisher Scientific), CV and EIS. The synthesized COF-based hybrid nanocomposite and constituent materials were subjected to FTIR in the scan range of 600–4000 cm⁻¹ using a Thermo Fischer Scientific (Nicolet 6700, USA) spectrometer. Polymorphism, crystallinity, and molecular dynamics were analyzed using an In-Via RAMAN microscope (Renishaw, UK) at an excitation wavelength of 514 nm for 10 s. The XRD patterns were obtained using a PXRD PANalytical Xpert powder diffractometer (Malvern) at a scan range of 0–80. The thermostability of the synthesized material was examined *via* TGA (BXT-DSC-TGA-1250) at 25–800 °C under nitrogen atmosphere (heating rate: 10 °C min⁻¹). The particle size measurements were performed using a Zetasizer Nano ZS90 (Malvern, UK).

2.2. Synthesis of Ag₂O/g-C₃N₄-COOH@MA-DBB-COF nanocomposite

The g-C₃N₄ was synthesized following Ahmed *et al.*, 2020 with slight modification.⁴⁷ Melamine (15 g) was heated to 550 °C at a ramp rate of 5 °C min⁻¹ for 4 h. Afterwards, the obtained amber-colored product was ground into a fine powder. To prepare Ag₂O/g-C₃N₄, g-AgNO₃ (8.2 g) and C₃N₄ (250 mg) were sonicated in 40 mL distilled water for 10 min, followed by the addition of 6 mg of K₂HPO₄ at 80 °C. The product was dried in an oven at 60 °C for 24 h. The functionalization of Ag₂O/g-C₃N₄ was carried out following Rauf *et al.*, 2018 (ref. 48) with slight modification. The Ag₂O/g-C₃N₄ (1 mg mL⁻¹ distilled H₂O) dispersion was obtained through sonication. Subsequently, to obtain Ag₂O/g-C₃N₄-COOH, NaOH (0.3 g) and C₂H₃ClO₂ (0.2 g) were added to the above dispersion, and the mixture was used for electrochemical assay.

MA-DBB-COF was synthesized following Sahiner *et al.*, 2016 (ref. 49) with slight modification. Melamine (0.0939 g/5 mL DMSO) and 1,4-dibromobutane (136 μL) were heated with magnetic stirring at 150 °C for 2 h. The obtained tangerine-colored precipitate of MA-DBB-COF was dried in an incubator at 37 °C for 45 min and stored for subsequent use.

2.3. Fabrication of electrochemical immunosensor (PGE/Ag₂O/g-C₃N₄-COOH@MA-DBB-COF)

The COF-based electroactive nanocomposite Ag₂O/g-C₃N₄-COOH@MA-DBB-COF was prepared by adding Ag₂O/g-C₃N₄-COOH (1 mg) and MA-DBB-COF (0.4 mg) to distilled water (1 mg Ag₂O/g-C₃N₄-COOH + 0.4 mg COF mL⁻¹), followed by sonication for 3–4 min. The surface of the modified working electrode (PGE/Ag₂O/g-C₃N₄-COOH@MA-DBB-COF) was fabricated by

incubating PGE in 10 μL of the nanocomposite (Ag₂O/g-C₃N₄-COOH@MA-DBB-COF) for 30 min and then allowing it to dry. Following the same procedure, PGE/Ag₂O/g-C₃N₄ and PGE/Ag₂O/g-C₃N₄-COOH were also fabricated, and DPV of all fabricated electrodes was performed (−0.2–0.5 V). As the designed immunosensor offers immobilization support to the bio-receptors through its functionalization feature, anti-AFM₁ antibody was conjugated to the carboxylic group on the electrode surface. This was carried out by incubating a mixture of 10 μL NHS (25 mM), EDC (100 mM), and the optimized anti-AFM₁ antibody concentration (1/4000 unit in PBS from a stock solution (6.6 mg mL⁻¹)) was used in further experimentation. Subsequently, 1% BSA was used as a blocking protein for 30 min at the surface of the anti-AFM₁-antibody-immobilized fabricated PGE.

2.4. Milk sample analysis using the designed electrochemical immunosensor and HPLC

A stock solution of AFM₁ (1 μL mL⁻¹ PBS) from 1.54 μM AFM₁ in acetonitrile was prepared and stored at −20 °C. The working standard solutions of 0.03–1000 fg mL⁻¹ prepared from the stock solution were used, and calibration curve was obtained by plotting the peak currents *vs.* the concentration of AFM₁. The LOD was calculated using the standard deviation of the response and the slope of the calibration curve, expressed as LOD = 3.3σ/S, where σ represents the standard deviation and S is the slope of the calibration curve.

The milk sample (5 mL) was centrifuged at 2000 rpm/20 min to remove fats. Subsequently, different concentrations of AFM₁ standards (6, 420 and 910 fg mL⁻¹) were spiked into the skimmed milk sample. Finally, the designed immunosensor was utilized to analyze the extract to study the viability of the proposed sensor in the food matrix.

To cross-validate the analytical performance of the designed immunosensor, HPLC (Prominence™, Shimadzu®, Kyoto, Japan) analysis of AFM₁ was also performed. The method was established with standard solution of AFM₁. A spectrofluorometer detector RF-10AXL® (Shimadzu, Japan) set at 365 nm excitation and 425 nm emission wavelengths was used. The isocratic mobile phase (20:60:20) of acetonitrile:water:methanol was used at a flow rate of 1.5 mL min⁻¹ 10 μL was the injection volume using a Rheodyne® manual sample injector. Sample cleanup was carried out using immunoaffinity columns (Afla star company, Australia). Milk samples from twenty different sites of local markets were collected and tested for the presence/absence of AFM₁ through both HPLC and the designed immunosensor.

3. Results and discussion

3.1. Surface characterization

Fig. 1A shows the comparative FTIR spectra of the synthesized materials, g-C₃N₄ and Ag₂O/g-C₃N₄. The sharp peak at 807 cm⁻¹ can be assigned to breathing mode vibrations, which are a characteristic feature of triazine rings, and the peaks at 1530 and 1640 cm⁻¹ can be attributed to C=N stretching.^{50,51} In the

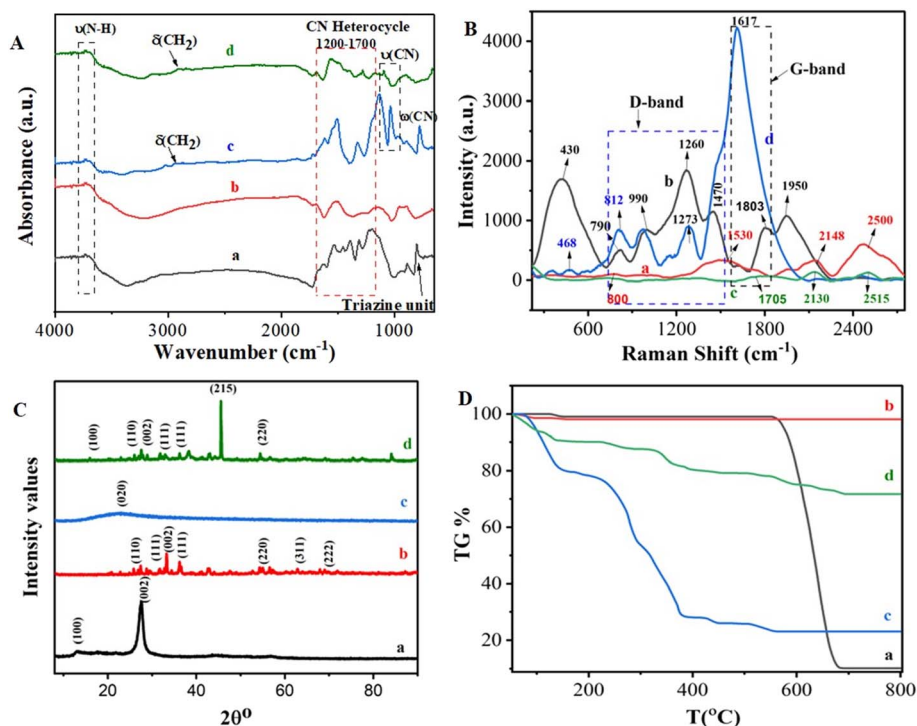


Fig. 1 (A) FTIR spectra, (B) Raman spectra, (C) XRD patterns, and (D) thermogravimetric analysis of (a) $g\text{-C}_3\text{N}_4$, (b) $\text{Ag}_2\text{O}/g\text{-C}_3\text{N}_4\text{-COOH}$, (c) MA-DBB-COF and (d) $\text{Ag}_2\text{O}/g\text{-C}_3\text{N}_4\text{-COOH}@$ MA-DBB-COF.

absorption spectra of $\text{Ag}_2\text{O}/g\text{-C}_3\text{N}_4$ (b), relatively sharp peaks were observed between $1400\text{--}1600\text{ cm}^{-1}$. The broad peak in the region $2500\text{--}3500\text{ cm}^{-1}$ was less intense and wider due to Ag_2O loading in the $\text{Ag}_2\text{O}/g\text{-C}_3\text{N}_4$ nanocomposite. As is evident in the FTIR spectrum of $\text{Ag}_2\text{O}/g\text{-C}_3\text{N}_4$ in Fig. 1A, the absorption spectrum of $g\text{-C}_3\text{N}_4$ showed peak shifts in the region $800\text{--}1700\text{ cm}^{-1}$, which were attributed to the coordination linking of Ag and N atoms, indicating successful incorporation of Ag_2O in $g\text{-C}_3\text{N}_4$.^{47,52} Furthermore, the FTIR spectra of MA-DBB-COF (c), and $\text{Ag}_2\text{O}/g\text{-C}_3\text{N}_4\text{-COOH}@$ MA-DBB-COF (d) are presented in Fig. 1A, and the details of the peaks are given in Table S1.† In the spectrum of $\text{Ag}_2\text{O}/g\text{-C}_3\text{N}_4\text{-COOH}@$ MA-DBB-COF (d), the peaks ($700\text{--}1550\text{ cm}^{-1}$) were less sharp, indicating loading of $\text{Ag}_2\text{O}/g\text{-C}_3\text{N}_4$ on the MA-DBB-COF surface. Sharp peaks at 770 , 1022 and 1130 cm^{-1} in the absorption spectrum of MA-DBB-COF (c) are representative of ring-out-of-plane deformations, and were broader and shifted to higher intensity for $\text{Ag}_2\text{O}/g\text{-C}_3\text{N}_4\text{-COOH}@$ MA-DBB-COF (d). To confirm the successful synthesis, structural changes were observed through Raman spectrographs (Fig. 1B). The graphitic and defect behavior is represented by the characteristic G and D bands, and the intensities of the disorder and graphite band (ID/IG) of each reacting component and nanocomposite material (Table S2†). $g\text{-C}_3\text{N}_4$ displayed a D-band at 800 cm^{-1} of the *s*-triazine unit. In the case of $\text{Ag}_2\text{O}/g\text{-C}_3\text{N}_4\text{-COOH}$, the relatively intense peak at 430 cm^{-1} indicates Ag_2O incorporated on the surface. The numerous newly observed peaks at 790 , 990 , 1260 , 1470 , 1803 and 1950 cm^{-1} represent interfacial interaction between Ag_2O and $g\text{-C}_3\text{N}_4\text{-COOH}$.^{47,53} In the spectra of MA-DBB-COF, the peak

at 1705 cm^{-1} can be assigned to aromatic C–N stretching vibrations, whereas the peaks at 2130 cm^{-1} and 2515 cm^{-1} indicate C=N bending modes. In the final COF-based nanocomposite, $\text{Ag}_2\text{O}/g\text{-C}_3\text{N}_4\text{-COOH}@$ MA-DBB-COF, the incorporation of Ag_2O is represented by the peak at 468 cm^{-1} and that of triazine subunit by the peak at 812 cm^{-1} . There is a gradual increase in the ID/IG ratio from $g\text{-C}_3\text{N}_4$ to $\text{Ag}_2\text{O}/g\text{-C}_3\text{N}_4\text{-COOH}@$ MA-DBB-COF, exhibiting more defects and less graphitic behavior in the final composite material, as shown in Table S2.†

The crystallinity and phases of the $g\text{-C}_3\text{N}_4$ (a), $\text{Ag}_2\text{O}/g\text{-C}_3\text{N}_4$ (b), MA-DBB-COF (c) and $\text{Ag}_2\text{O}/g\text{-C}_3\text{N}_4\text{-COOH}@$ MA-DBB-COF (d) were characterized using XRD (Fig. 1C). In $g\text{-C}_3\text{N}_4$, the two diffraction peaks appearing at 13.1° and 27.5° were suggested to correspond to the (100) and (002) planes of hexadic $g\text{-C}_3\text{N}_4$ (JCPDS 87-1526), respectively.⁵⁴ In the $\text{Ag}_2\text{O}/g\text{-C}_3\text{N}_4$ (b) nanocomposites, both the peaks were less intense, and a few additional peaks observed at various $2\theta^\circ$ values of were attributed to the (110), (111), (220), (311) and (222) diffraction planes of the cubic crystal phase (JCPDS 41-1104).⁵⁵ This shows the successful incorporation of Ag_2O in $g\text{-C}_3\text{N}_4$. In the XRD pattern of the synthesized COF (c), there was a broad peak extending from 14° to 34° , which was suggested to be (020). The final composite material, $\text{Ag}_2\text{O}/g\text{-C}_3\text{N}_4\text{-COOH}@$ MA-DBB-COF (d) was found to be crystalline. It showed peaks referring to the (100), (110), (002), (111) and (220) refractive angles. Thermogravimetric analysis was performed to analyze the thermal stability of the synthesized composite material (Fig. 1D). $g\text{-C}_3\text{N}_4$ exhibits (a) an onset 1% weight loss between $123\text{--}149^\circ\text{C}$. This may be

attributed to loss of water trapped in the interstices. $g\text{-C}_3\text{N}_4$ remained intact between 150–559 °C, and an 87.7% decrease in weight was observed between 599 and 681 °C with only 0.1% further weight loss between 681 and 800 °C. As shown in Fig. 1D(b), $\text{Ag}_2\text{O}/g\text{-C}_3\text{N}_4\text{-COOH}$ showed 2% weight loss at 48–98 °C followed by only 0.34% decrease in weight between 129 and 154 °C. The entirely different TGA profiles of $g\text{-C}_3\text{N}_4$ and $\text{Ag}_2\text{O}/g\text{-C}_3\text{N}_4$ indicate the successful synthesis of $\text{Ag}_2\text{O}/g\text{-C}_3\text{N}_4$. MA-DBB-COF (c) showed three-phase degradation: a first phase at 72–150 °C, a second at 150–393 °C and a third phase between 390–561 °C. Finally, as shown in Table S3,† the $\text{Ag}_2\text{O}/g\text{-C}_3\text{N}_4\text{-COOH}@MA\text{-DBB-COF}$ (d) displayed a different TGA profile, with a 10% weight loss in the range 100–150 °C, followed by 11% weight loss between 232 and 454 °C. Lastly, between 506 and 692 °C, only 7.3% weight loss was observed. Afterwards, the composite remained intact at up to 800 °C. Thus, a highly thermostable composite was synthesized, as 72% of the composite did not degrade even at very high temperature.

Zeta potential measurements were performed to study the surface modifications of the synthetic materials. The particle size of the final composite material $\text{Ag}_2\text{O}/g\text{-C}_3\text{N}_4\text{-COOH}@MA\text{-DBB-COF}$ was found to be 442.6 nm. All the contributing materials intrinsically had negative zeta potentials. However, upon acidification, the zeta potential of $\text{Ag}_2\text{O}/g\text{-C}_3\text{N}_4\text{-COOH}$ increased to -78.1 mV from -0.421 mV for $g\text{-C}_3\text{N}_4$ due to the development of the negatively charged surface attributed to -COO^- . MA-DBB-COF and $\text{Ag}_2\text{O}/g\text{-C}_3\text{N}_4\text{-COOH}@MA\text{-DBB-COF}$ showed zeta potentials of -7.02 mV and -80.4 mV, respectively. Particles with a zeta potential $>+30$ mV or >-30 mV are considered stable; thus, a stable nanocomposite was prepared.

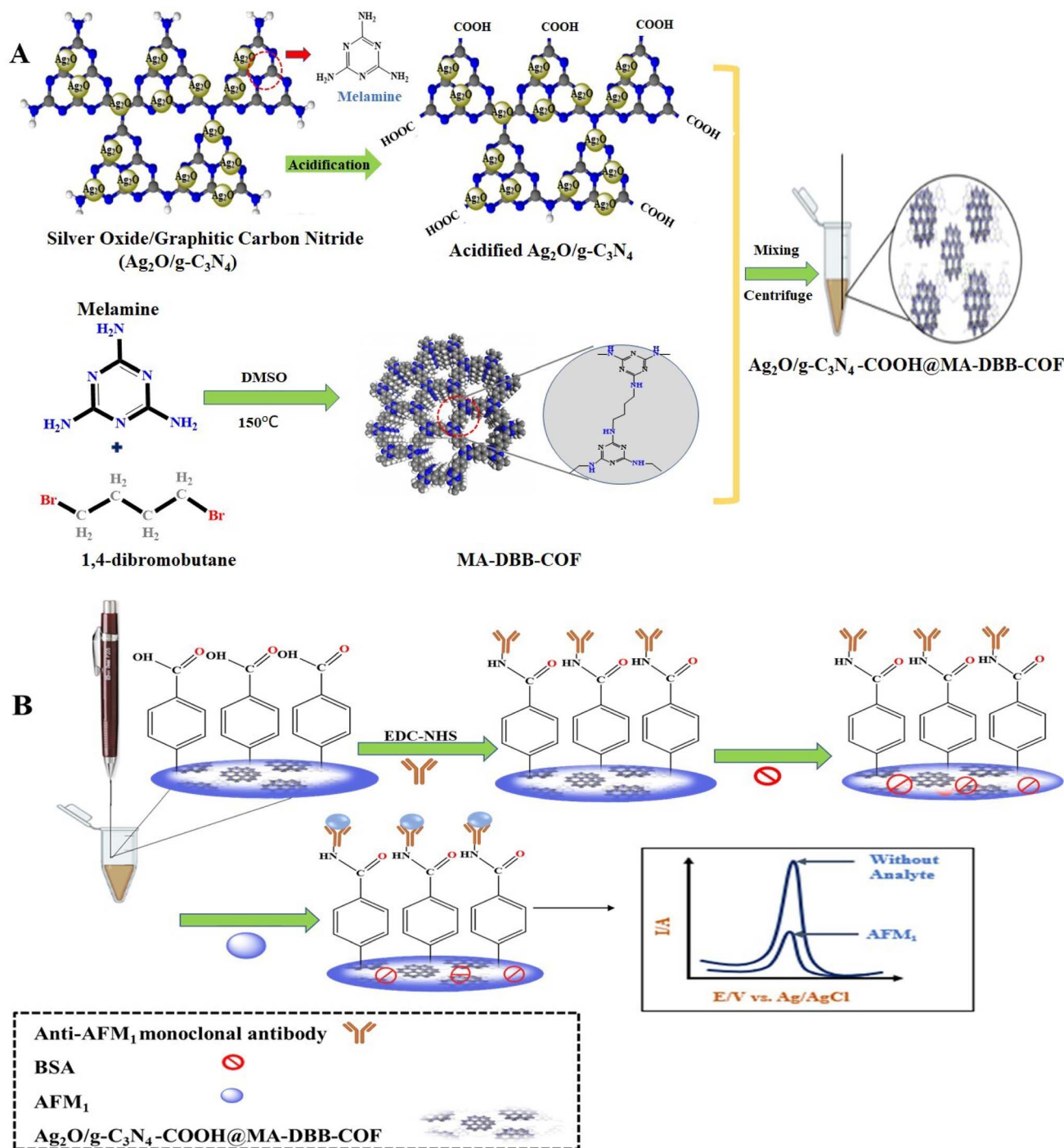
3.2. Principle design of electrochemical immunosensor

The ability of the synthesized COF-based electroactive nanocomposite material to undergo electrooxidation, and to offer immobilization support to the bioreceptor and signal amplification through enhanced electrical conductivity, are the basic principles of the designed label-free electrochemical immunosensor. The presence of electroactive Ag in the nanocomposite generates a sharp oxidation signal response in an electrochemically inactive PBS solution. The working principle of the designed electrochemical immunosensor and electrochemical response of the designed sensing platform are displayed in Scheme 1. The unmodified PGE did not generate any electrical signal. Upon customization of the PGE with the $\text{Ag}_2\text{O}/g\text{-C}_3\text{N}_4$ hybrid nanocomposite, an oxidation peak at a potential of $+0.14$ V was observed, as is evident in Fig. S1(a),† which affirmed the electroactive nature of the integrated nanocomposite.^{56,57} Acidification of $\text{Ag}_2\text{O}/g\text{-C}_3\text{N}_4$ to $\text{Ag}_2\text{O}/g\text{-C}_3\text{N}_4\text{-COOH}$ not only resulted in a decrease in the electrical signal, but also added the feature of biocompatibility. $\text{Ag}_2\text{O}/g\text{-C}_3\text{N}_4\text{-COOH}$ was integrated with MA-DBB-COF, and the resulting modified PGE/ $\text{Ag}_2\text{O}/g\text{-C}_3\text{N}_4\text{-COOH}@MA\text{-DBB-COF}$ showed significant signal amplification of the electro-oxidation signal of Ag^+ , as shown in Fig. S1(c).† Herein, the material modification to fabricate the transducer surface, particularly with COF, was relatively conductive in nature.⁵⁸ The -COOH group in $\text{Ag}_2\text{O}/g\text{-C}_3\text{N}_4\text{-COOH}$

of the modified PGE was activated by the cross-linker EDC/NHS to develop an amide linkage with the anti-AFM₁ antibody for aligned orientation. The scope of the study can be extended in terms of material modification and wide-scale sensing application, as $\text{Ag}_2\text{O}/g\text{-C}_3\text{N}_4$ can be functionalized to $\text{Ag}_2\text{O}/g\text{-C}_3\text{N}_4\text{-NH}_2$, as well as the $\text{Ag}_2\text{O}/g\text{-C}_3\text{N}_4\text{-COOH}$ presented in this report. The -COOH in the modified nanocomposite can develop an amide linkage with the -NH_2 terminal of various biorecognition molecules; the antibody anti-AFM₁ was chosen to establish the working principle in the present study. Subsequently, BSA was used as a blocking agent to avoid any nonspecific adsorption at the surface of the anti-AFM₁-antibody-bound fabricated PGE. The decrease in the electrical signal due to complexation between the bioreceptor and target analyte is the basis of detection. PGE was customized with $\text{Ag}_2\text{O}/g\text{-C}_3\text{N}_4\text{-COOH}@MA\text{-DBB-COF}$ to serve as a multifunctional electrochemical transduction platform. AFM₁ was used as a target analyte to validate the working principle of the designed transducer. The DPV response of the modified PGE decreased in the presence of AFM₁, indicating that the anti-AFM₁-antibody-immobilized nano-transducer interface was electroreceptive, complexing with AFM₁. There was a proportional decrease in the electrooxidation signal of Ag^+ of the designed modified PGE with increasing concentrations of AFM₁. This decrease can be used for quantitative estimation of AFM₁.

3.3. Electrochemical surface characterization of the receptor surface

CV, EIS and FE-SEM images were used to characterize each step of fabrication for the development of the immunosensor. The step-wise consecutive measurements were carried out against 0.1 mM ferri/ferrocyanide as a reversible redox probe, at a 50 mV s^{-1} scan rate, as shown in Fig. 2A. The peak-to-peak separation and variation in peak current at each step of PGE fabrication relate to the resistance and heterogeneous electron transfer rate. The bare PGE showed a couple of anodic and cathodic peaks. After the deposition of $\text{Ag}_2\text{O}/g\text{-C}_3\text{N}_4\text{-COOH}@MA\text{-DBB-COF}/\text{EDC-NHS}$ on PGE, there was an increase in the electron transfer rate, as indicated by the decrease in the peak-to-peak separation value. The fabricated PGE showed an increased current response compared to unmodified PGE. Upon the covalent binding of anti-AFM₁ antibody on the modified PGE, there was a decrease in the CV response of the redox couple, as the bulky anti-AFM₁ antibody molecule may create hindrance in electron transfer. The next fabrication step was BSA treatment to block nonspecific adsorption, which further decreased the CV response. The hindered electron-transfer kinetics of ferri/ferrocyanide were observed in the interaction of AFM₁ with the modified PGE, causing blockage of the redox peak. The EIS results are consistent with CV surface characterization, as displayed in Fig. 2A and B. There was an increase in electron-transfer resistance, confirming that designed approach is suitable for the detection of AFM₁. The data regarding the electroactive surface area and peak potential difference ΔE_p are presented in Table S4.† The bare PGE had an electroactive surface area of 0.024 cm^2 , whereas modification of the electrode



Scheme 1 (A) Preparation of acidified $\text{Ag}_2\text{O}/\text{g-C}_3\text{N}_4\text{-COOH@MA-DBB-COF}$; (B) immunosensor fabrication.

with $\text{Ag}_2\text{O}/\text{g-C}_3\text{N}_4\text{-COOH@MA-DBB-COF}/\text{EDC-NHS}$ increased the electroactive surface to 0.031 cm^2 . Further, the deposition of anti- AFM_1 antibody on $\text{PGE}/\text{Ag}_2\text{O}/\text{g-C}_3\text{N}_4\text{-COOH@MA-DBB-COF}$ decreased the electroactive surface area (0.021 cm^2) compared to that of the modified immunosensor.

The electrochemical signal of Ag^+ in the designed nanocomposite material was monitored through DPV in 0.1 M PBS (pH = 7.0) as shown in Fig. S1 & S2.† Anti- AFM_1 antibody deposition followed by AFM_1 binding resulted in successive

decreases in the electrical signal, which formed the basis for quantitative determination.

In order to examine the structural changes at molecular level during the different fabrication steps of the immunosensor, the surface morphology was studied using FE-SEM to show the modification in the surface nature. It can be observed from Fig. 2C that the unmodified PGE has distinct morphology in comparison to the other stages, *i.e.*, when PGE was modified with EDC-NHS and BSA anti- AFM_1 antibody and AFM_1 were

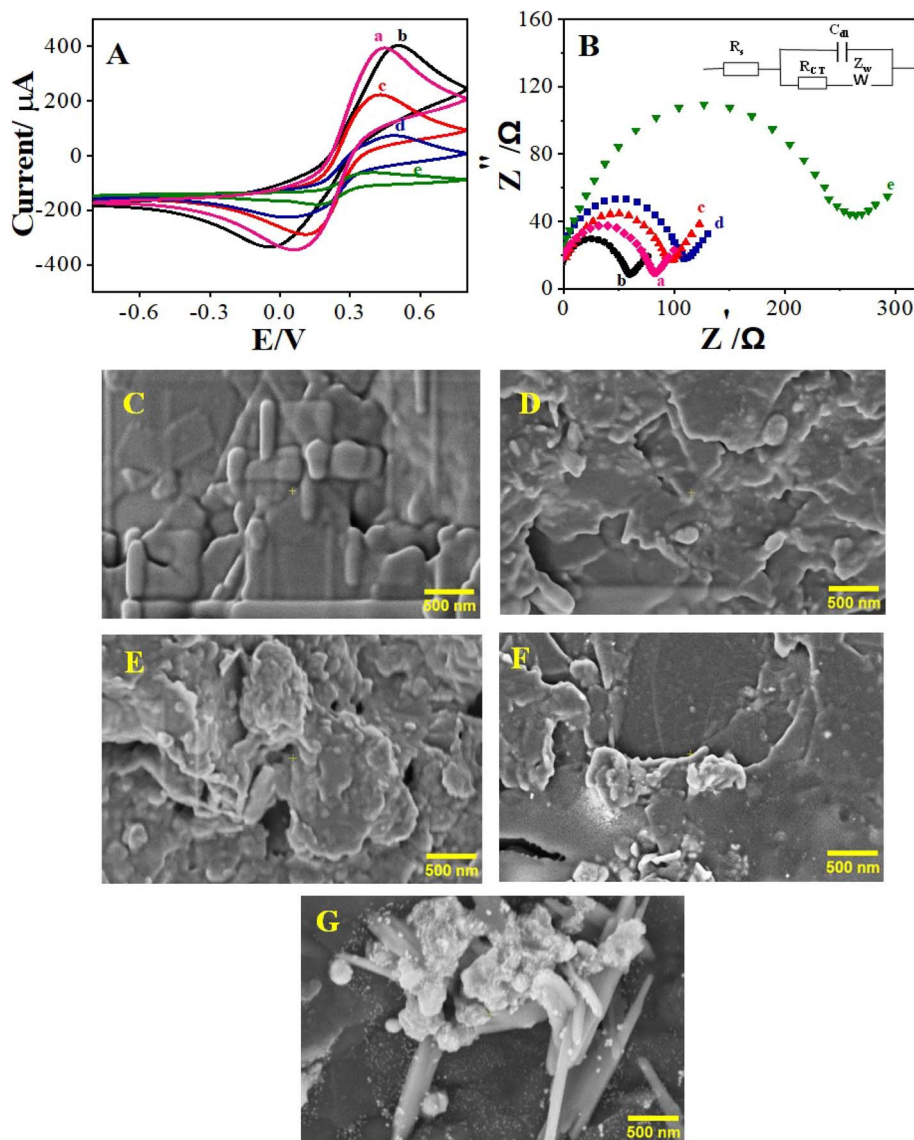


Fig. 2 (A) Cyclic voltammograms and (B) electrochemical impedance spectroscopy (Nyquist plot) of 0.1 M $[\text{Fe}(\text{CN})_6]^{3-/4-}$ at a scan rate of 50 mV s^{-1} for the (a) bare electrode, (b) EDC-NHS/Ag₂O/g-C₃N₄-COOH@MA-DBB-COF/PGE, (c) anti-AFM₁ antibody/EDC-NHS/Ag₂O/g-C₃N₄-COOH@MA-DBB-COF/PGE, (d) BSA/anti-AFM₁ antibody/EDC-NHS/Ag₂O/g-C₃N₄-COOH@MA-DBB-COF/PGE and (e) AFM₁/BSA/anti-AFM₁ antibody/EDC-NHS/Ag₂O/g-C₃N₄-COOH@MA-DBB-COF/PGE. FE-SEM images of the step-wise modification of the pencil graphite electrode for the (C) bare electrode, (D) EDC-NHS/Ag₂O/g-C₃N₄-COOH@MA-DBB-COF/PGE, (E) anti-AFM₁ antibody/EDC-NHS/Ag₂O/g-C₃N₄-COOH@MA-DBB-COF/PGE, (F) BSA/anti-AFM₁ antibody/EDC-NHS/Ag₂O/g-C₃N₄-COOH@MA-DBB-COF/PGE and (G) AFM₁/BSA/anti-AFM₁ antibody/EDC-NHS/Ag₂O/g-C₃N₄-COOH@MA-DBB-COF/PGE.

used to test the performance of the designed sensor. The distinct morphological changes are further evident in the FE-SEM images of the fabrication steps in Fig. S3.† The surface modification *via* their step-wise application on the designed immunosensor was also compared using FE-SEM. It can also be observed that the surface roughness of PGE increased after the deposition of EDC-NHS/Ag₂O/g-C₃N₄-COOH@MA-DBB-COF and was further enhanced upon the application of anti-AFM₁ antibody/EDC-NHS/Ag₂O/g-C₃N₄-COOH@MA-DBB-COF. Similarly, the surface morphology of the designed immunosensor changed upon the addition of anti-AFM₁ antibody followed by AFM₁.

3.4. Optimization of experimental parameters

To improve the analytical performance of the developed immunosensor, the optimization of several factors is critical. Analytical variables like incubation time, concentration of the composite material, bioreceptor concentration and analyte incubation time can substantially affect the performance of the sensor. The analytical performance of the designed immunosensor can be affected by the incubation time of the materials constituting the COF-based nanocomposite material. Different time intervals (5–60 min) for the incubation of Ag₂O/g-C₃N₄-COOH on PGE were observed. There was a proportional increase in the electrical response with gradual increase in incubation

time. After 30 min, there was a decrease in the electrical signal, as shown in Fig. S4(A).† At 30 min, the maximum electro-oxidation of Ag was accomplished; the subsequent decrease in the electrical signal indicates the reversibility of the reaction. Fig. S4(B)† represents the effect of the concentration of MA-DBB-COF on the peak current in the 0.1 M PBS. Different concentrations (0.1–0.5 mg mL⁻¹) of MA-DBB-COF were used, and the highest electrical response was observed at 0.4 mg mL⁻¹ of MA-DBB-COF. Afterwards, the excessive deposition of MA-DBB-COF on the electrode surface led to a steady electron transfer rate.

The electrical signal is directly influenced by the variation in bioreceptor concentration. Therefore, different concentrations (1/1000 to 1/10 000 units in PBS) of anti-AFM₁ antibody were immobilized at the modified PGE/Ag₂O/g-C₃N₄-COOH@MA-DBB-COF electrode, and DPVs were recorded to determine the optimum response. The optimum working dilution of anti-AFM₁ antibody was found to be 1/4000 unit in PBS, which caused the maximum decrease in the electrical signal, as shown in Fig. S4D.† Further non-specific adsorption of anti-AFM₁ antibody on PGE/Ag₂O/g-C₃N₄-COOH@MA-DBB-COF was prevented by using 1% BSA solution for 30 min. The incubation time for anti-AFM₁ antibody and AFM₁ were optimized by considering different time intervals (5, 15, 30, 45 and 60 min). The optimum incubation time for anti-AFM₁ antibody was 30 min (Fig. S4C†). AFM₁ exhibited maximum immobilization of anti-AFM₁ antibody at 30 min, as shown in Fig. S4E.†

3.5. Electrochemical detection of AFM₁

Control experiments were performed by gradually integrating Ag₂O/g-C₃N₄, Ag₂O/g-C₃N₄-COOH and Ag₂O/g-C₃N₄-COOH@MA-DBB-COF on PGE, as shown in Fig. S1.† The output signal at +0.14 V attributed to Ag in Ag₂O/g-C₃N₄ decreased upon functionalization due to the repulsion caused by the negative charge of the carboxylic group. In contrast, a substantial increase in the output signal was observed after the deposition of MA-DBB-COF on PGE/Ag₂O/g-C₃N₄-COOH, as shown in Fig. S1(c).† Subsequently, the cross-linker EDC-NHS was used to activate the -COOH group, followed by covalent immobilization of anti-AFM₁ antibody, as shown in Fig. S2.†,⁵⁹

The designed PGE/Ag₂O/g-C₃N₄-COOH@MA-DBB-COF/EDC-NHS/anti-AFM₁ antibody immunosensor was exposed to different concentrations of AFM₁ to monitor the binding between the anti-AFM₁-antibody-modified probe and AFM₁. Upon the addition of AFM₁, there was a substantial decrease in the oxidation signal representing AFM₁ binding on the transducer surface. The results confirmed that the greater the amount of AFM₁ bound to immunosensor, the smaller the oxidation signal of the designed immunosensor. Hence, there was a decrease in the number of active sites, and the oxidation current peak at 0.13 V was decreased by increasing the amount of AFM₁, as shown in Fig. 3A. Thus, there exists a correlation between the concentration of AFM₁ and the variation in the oxidation peak intensity. Different known concentrations of AFM₁ (0.03–1000 fg mL⁻¹) were assessed, and DPV was employed for recording the response. A substantial decrease in

the electrical response with increasing concentration is shown in Fig. 3A. The decrease in the oxidation peak is proportional to the increasing concentration of AFM₁. Therefore, the designed immunosensor can be employed for quantitative analysis. The obtained LOD was 0.01 fg mL⁻¹ with a linear range of 0.03–1000 fg mL⁻¹ for AFM₁, as depicted in Fig. 3A and B, representing the excellent viability of the designed sensor. A comparison of the analytical performance of the BSA/anti-AFM₁ antibody/EDC-NHS/Ag₂O/g-C₃N₄-COOH@MA-DBB-COF/PGE immunosensor with other electrochemical sensors recently reported in the literature for the detection of AFM₁ is presented in Table S5.†

3.6. Specificity of the AFM₁ immunosensor

Intense false electrochemical signals can be generated by nonspecific interactions. Label-free detection methods are affected by these interfering nonspecific interactions. It was necessary to ensure that the change in the oxidation signal was caused entirely by the specific interaction between anti-AFM₁ antibody on the transducer surface and AFM₁, and not by the non-specific adsorption of AFM₁. Thus, the specificity of the designed immunosensor for AFM₁ was assessed *versus* selected interfering mycotoxins such as OTA, OTB, AFB₁ and ZEN, as shown in Fig. 3C. The experiment was carried out by incubating the developed immunosensor in concentrations of the interfering analytes that were 10 times higher than the concentration of AFM₁. The findings clearly indicate the selective response of the immunosensor PGE/Ag₂O/g-C₃N₄-COOH@MA-DBB-COF/EDC-NHS/anti-AFM₁ antibody toward AFM₁ analysis.

3.6.1. Reproducibility, accuracy and stability study of AFM₁ immunosensor. As the proposed COF-based electroactive probe is cost effective, the designed immunosensor will be disposable and easy to use. Inter-assay accuracy and precision were used to estimate the reproducibility of the designed immunosensor. Six fabricated electrodes were used to estimate the accuracy and reproducibility of the COF-based nanocomposite probe with a constant concentration of AFM₁ under similar experimental conditions. The calculated percentage relative standard deviation (R. S. D. %) values of 1.8% and 1.9% demonstrated the fabrication stability and adequate precision, respectively. With a negligible loss in activity (S. D. 1.6%), the designed immunosensor maintained its electrochemical response over an extended period of time (stored at 4 °C) to serve as a ready-to-use device for single-step analysis of AFM₁. Fig. 3D shows the response of the sensor over two weeks (representative); however, response stability was observed up to six months without significant loss in the signal. The extended stability can be attributed to the amide linkage between the -COOH group of the nanocomposite and the terminal -NH₂ group of the anti-AFM₁ antibody. These findings indicate the excellent stability and reproducibility of the designed transducer surface.

3.7. Milk sample analysis

As an in-field application, the proposed probe was used to detect AFM₁ in milk samples. To study the matrix effect, different concentrations (6 420 910 fg mL⁻¹) of AFM₁ were spiked into milk samples, and the corresponding recovery

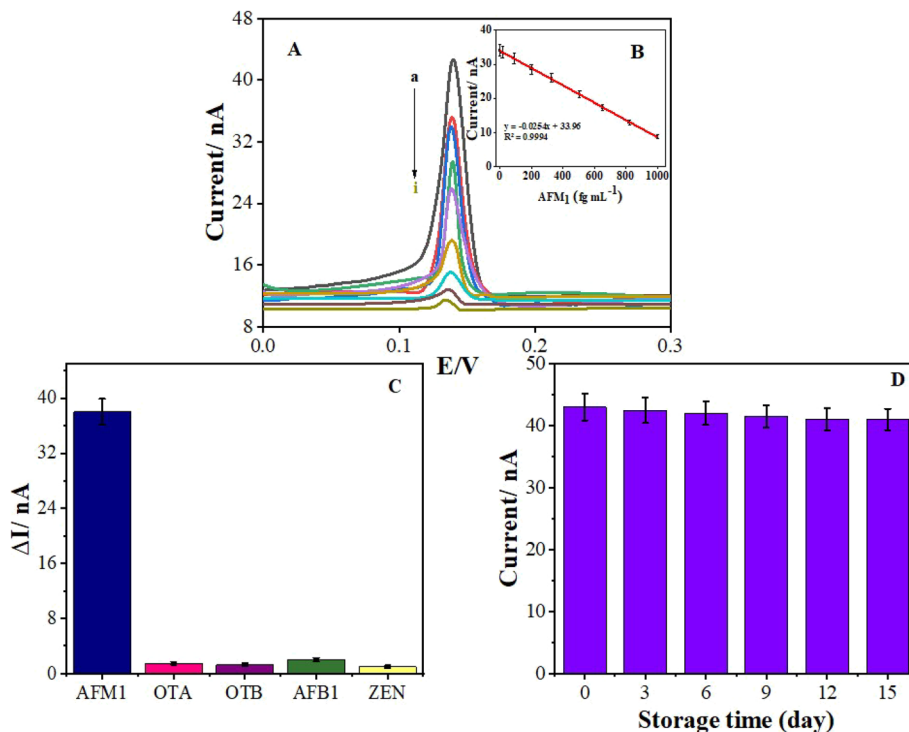


Fig. 3 (A) Differential voltammograms for different concentrations of the analyte: (a) 0.03, (b) 16, (c) 90, (d) 200, (e) 328 (f) 505, (g) 650, (h) 820, and (i) 1000 fg mL^{-1} . (B) Calibration curve for AFM_1 concentration. (C) Specificity of the immunosensor and (D) stability of the immunosensor.

Table 1 Accuracy obtained with the proposed electrochemical immunosensor^a

Milk sample	AFM_1 added (fg mL^{-1})	AFM_1 found (fg mL^{-1})	R. S. D. %	R. E. %	R %
1	6	5.836	1.95	2.73%	97.28%
2	420	428.01	1.33	1.90%	101%
3	910	933.85	1.82	2.52%	102.62%

^a R. E. % = relative error; R% = recovery percentage.

values were calculated, as presented in Table 1. The observed recovery percentages were <97%, with R. S. D. values of approximately >2.0% ($n = 3$), which represents the acceptable accuracy of the proposed immunosensor, as shown in Table 1.

Furthermore, to validate the performance of designed immunosensor, established HPLC method for the detection of AFM_1 was used in parallel. Fig. S5† is the representative chromatogram of standard AFM_1 obtained with the established HPLC based method. Twenty different sites were selected in the local market to collect the milk samples for screening of AFM_1 via immunosensor and HPLC method. Thirteen samples were found AFM_1 positive with both the methodologies (0.5–0.8 ng mL^{-1}). While seven were AFM_1 negative following HPLC method, however, out of these seven samples, five were AFM_1 positive with the designed immunosensor (350–800 fg mL^{-1}). This can be attributed to lower range detection capability of the proposed immunosensor in comparison to that of HPLC based method that permitted to detect lower AFM_1 concentrations lower than the range of HPLC based method. The remaining

two samples were found AFM_1 negative with the proposed immunosensor, and were used for the recovery studies. These results show the successful application of the developed multifunctional electrochemical sensor to screen the contaminated milk samples.

4. Conclusion

This study reports a novel approach for the successful design of an easy to use, one-step, highly sensitive and selective electrochemical immunosensor for the detection of AFM_1 in milk samples. The designed sensing platform was composed of a COF-based electroactive hybrid nanocomposite material, $\text{Ag}_2\text{O/g-C}_3\text{N}_4\text{-COOH@MA-DBB-COF}$, fabricated on PGE with an analyte-specific antibody. The COF-based electroactive nanocomposite material served as a multitasking probe offering relative conductivity, immobilization support, and an electro-oxidation signal. The principle for the immunosensor design follows the hypothesis of complex formation between anti-

AFM₁-monoclonal antibody and AFM₁ leading to decrease in the oxidation signal through steric crowding. Compared to existing electrochemical immunosensors, the proposed design offers a multifunctional, single-step and highly sensitive sensing platform. The applicability of the immunosensor for AFM₁ detection was validated by analysis of local market milk samples. The proposed transducer design can be used as a prototype sensing platform for the inexpensive and specific detection of AFM₁ in the screening of milk samples.

Data availability

The data supporting this article have been included as part of the ESI.†

Author contributions

Iram Naz: contributed to writing original draft, study conception, data curation, formal analysis, project administration, validation, and visualization. Akhtar Hayat: contributed to the study conception, formal analysis, funding acquisition, methodology, resources, supervision, writing-review and editing, Farhat Jubeen: contributed to the writing original draft, study conception, data curation, formal analysis, funding acquisition, investigation, project administration, resources, supervision, validation, and visualization. Sadia Asim contributed to the software and formal analysis. All authors read and approved the final manuscript. Abida Kausar: contributed to the software and formal analysis.

Conflicts of interest

The authors declare that they have no known competing interests.

Acknowledgements

The authors of the present study are highly thankful for financial assistance from the (i) Ministry of Science and Technology, Government of Pakistan for the developmental grant entitled as “Establishment of Center for Advance Technologies in Biomedical Material” under its knowledge economy initiative and (ii) Higher Education Commission of Pakistan through 8966/Federal/NRPU/R&D/HEC/2017.

References

- 1 F. Gaucheron, *J. Am. Coll. Nutr.*, 2011, **30**, 400s–409s.
- 2 B. Grenov, A. Larnkjær, C. Mølgaard and K. F. Michaelsen, in *Global Landscape of Nutrition Challenges in Infants and Children: 93rd Nestlé Nutrition Institute Workshop March 2019*, ed. K. F. Michaelsen, L. M. Neufeld, A. M. Prentice and S. Karger, AG, Kolkata, 2020, vol. 93.
- 3 V. Awasthi, S. Bahman, L. K. Thakur, S. K. Singh, A. Dua and S. Ganguly, *Indian J. Public Health*, 2012, **56**, 95–99.
- 4 S. Firdous, A. Ashfaq, S. J. Khan and N. Khan, *Food additives & contaminants. Part B, Surveillance*, 2014, **7**, 95–98.

- 5 N. Ali, *Toxicol Rep*, 2019, **6**, 1188–1197.
- 6 A. M. Macri, I. Pop, D. Simeanu, D. Toma, I. Sandu, L. L. Pavel and O. S. Mintas, *Microorganisms*, 2020, **9**, 61.
- 7 I. Naeem, A. Ismail, A. U. Rehman, Z. Ismail, S. Saima, A. Naz, A. Faraz, C. A. F. de Oliveira, N. Benkerroum, M. Z. Aslam and R. Aslam, *Int. J. Environ. Res. Public Health*, 2022, **19**, 3404.
- 8 P. Khazaeli, M. Mehrabani, M. R. Heidari, G. Asadikaram and M. Lari Najafi, *Iran. J. Public Health*, 2017, **46**, 1540–1545.
- 9 R. Shadjou, M. Hasanzadeh, M. Heidar-Poor and N. Shadjou, *J. Mol. Recognit.*, 2018, **31**, e2699.
- 10 S. Marchese, A. Polo, A. Ariano, S. Velotto, S. Costantini and L. Severino, *Toxins*, 2018, **10**, 214.
- 11 Q. Chen, M. Meng, W. Li, Y. Xiong, Y. Fang and Q. Lin, *Food Chem.*, 2023, **398**, 133848.
- 12 P. Malik, R. Gupta, V. Malik and R. K. Ameta, *Meas.: Sens.*, 2021, **16**, 100050.
- 13 A. A. Ismaiel, N. A. Tharwat, M. A. Sayed and S. A. Gameh, *J. Food Sci. Technol.*, 2020, **57**, 2182–2189.
- 14 B. D. Abera, A. Falco, P. Ibba, G. Cantarella, L. Petti and P. Lugli, *Sensors*, 2019, **19**, 3912.
- 15 S. S. Omar, *Ital. J. Food Saf.*, 2016, **5**, 5788.
- 16 A. M. Zakaria, Y. A. Amin, O. S. F. Khalil, E. Y. Abdelhiee and M. M. Elkamshishi, *J. Adv. Vet. Anim. Res.*, 2019, **6**, 197–201.
- 17 J. Ramesh, S. Ghadevaru and V. Sureshkumar, *Int. J. Curr. Microbiol. Appl. Sci.*, 2013, **2**, 373–377.
- 18 F. Jubeen, N. Zahra, Z. I. Nazli, M. K. Saleemi, F. Aslam, I. Naz, L. B. Farhat, A. Saleh, S. Z. Alshawwa and M. Iqbal, *Toxins*, 2022, **14**, 547.
- 19 A. Mateen, in *Aflatoxins*, ed. A. U. Lukman Bola, IntechOpen, Rijeka, 2021, Ch. 10, DOI: [10.5772/intechopen.98508](https://doi.org/10.5772/intechopen.98508).
- 20 S. C. Pei, Y. Y. Zhang, S. A. Eremin and W. J. Lee, *Food Control*, 2009, **20**, 1080–1085.
- 21 S. F. Ahmadi, M. Hojjatoleslami, H. Kiani and H. Molavi, *Food Chem.*, 2022, **373**, 131321.
- 22 Y.-H. Pang, L.-L. Guo, X.-F. Shen, N.-C. Yang and C. Yang, *Electrochim. Acta*, 2020, **341**, 136055.
- 23 N. Tarannum, M. N. Nipa, S. Das and S. Parveen, *Toxicol Rep*, 2020, **7**, 1339–1343.
- 24 X. Zhang, C.-R. Li, W.-C. Wang, J. Xue, Y.-L. Huang, X.-X. Yang, B. Tan, X.-P. Zhou, C. Shao, S.-J. Ding and J.-F. Qiu, *Food Chem.*, 2016, **192**, 197–202.
- 25 E. C. Dreaden, A. M. Alkilany, X. Huang, C. J. Murphy and M. A. El-Sayed, *Chem. Soc. Rev.*, 2012, **41**, 2740–2779.
- 26 K. Abhijith, K. Ragavan and M. Thakur, *Anal. Methods*, 2013, **5**, 4838–4845.
- 27 M. Tudorache and C. Bala, *Sensors*, 2008, **8**, 7571–7580.
- 28 S. Srivastava, V. Kumar, K. Arora, C. Singh, M. A. Ali, N. K. Puri and B. D. Malhotra, *RSC Adv.*, 2016, **6**, 56518–56526.
- 29 N. Gan, J. Zhou, P. Xiong, F. Hu, Y. Cao, T. Li and Q. Jiang, *Toxins*, 2013, **5**, 865–883.
- 30 G. Li, C. Liu, X. Zhang, P. Luo, G. Lin and W. Jiang, *Food Chem.*, 2021, **355**, 129443.
- 31 X. Tang, G. Catanante, X. Huang, J.-L. Marty, H. Wang, Q. Zhang and P. Li, *Food Chem.*, 2022, **383**, 132598.

- 32 S. Mousumi, in *Nanotechnology and the Environment*, ed. S. Mousumi, IntechOpen, Rijeka, 2020, Ch. 6, DOI: [10.5772/intechopen.93047](https://doi.org/10.5772/intechopen.93047).
- 33 J. Hári and B. Pukánszky, in *Applied Plastics Engineering Handbook*, ed. M. Kutz, William Andrew Publishing, Oxford, 2011, pp. 109–142, DOI: [10.1016/B978-1-4377-3514-7.10008-X](https://doi.org/10.1016/B978-1-4377-3514-7.10008-X).
- 34 X. An, X. Shi, H. Zhang, Y. Yao, G. Wang, Q. Yang, L. Xia and X. Sun, *New J. Chem.*, 2020, **44**, 1362–1370.
- 35 G. Kaur, S. Sharma, S. Singh, N. Bhardwaj and A. Deep, *ACS Omega*, 2022, **7**, 17600–17608.
- 36 J. Zhu, P. Xiao, H. Li and S. A. C. Carabineiro, *ACS Appl. Mater. Interfaces*, 2014, **6**, 16449–16465.
- 37 J. Low, B. Cheng, J. Yu and M. Jaroniec, *Energy Storage Mater.*, 2016, **3**, 24–35.
- 38 Q. Zhao, W. Wu, X. Wei, J. Shunli, T. Zhou, Q. Li and Q. Lu, *Sens. Actuators, B*, 2017, **248**, 673–681.
- 39 N. Mekgoe, N. Mabuba and K. Pillay, *Front. sens.*, 2022, **3**, 827954.
- 40 H. Zhang, Q. Huang, Y. Huang, F. Li, W. Zhang, C. Wei, J. Chen, P. Dai, L. Huang, Z. Huang, L. Kang, S. Hu and A. Hao, *Electrochim. Acta*, 2014, **142**, 125–131.
- 41 S. Munusamy, K. Sivaranjan, P. Sabhapathy, V. Narayanan, F. Mohammad and S. Sagadevan, *Synth. Met.*, 2021, **272**, 116669.
- 42 M. Afshari, M. Dinari and M. M. Momeni, *J. Electroanal. Chem.*, 2019, **833**, 9–16.
- 43 S. Vinoth, K. S. Shalini Devi and A. Pandikumar, *TrAC, Trends Anal. Chem.*, 2021, **140**, 116274.
- 44 V. Biju, *Chem. Soc. Rev.*, 2014, **43**, 744–764.
- 45 M. Holzinger, A. Le Goff and S. Cosnier, *Front. Chem.*, 2014, **2**, 63.
- 46 S. Chen, B. Yuan, G. Liu and D. Zhang, *Front. Chem.*, 2020, **8**, 601044.
- 47 A. Ahmed, A. Hayat, M. H. Nawaz, P. John and M. Nasir, *J. Colloid Interface Sci.*, 2020, **558**, 230–241.
- 48 S. Rauf, G. K. Mishra, J. Azhar, R. K. Mishra, K. Y. Goud, M. A. H. Nawaz, J. L. Marty and A. Hayat, *Anal. Biochem.*, 2018, **545**, 13–19.
- 49 N. Sahiner, S. Demirci and K. Sel, *J. Porous Mater.*, 2016, **23**, 1025–1035.
- 50 J. Liu, T. Zhang, Z. Wang, G. Dawson and W. Chen, *J. Mater. Chem.*, 2011, **21**, 14398–14401.
- 51 B. Fahimirad, A. Asghari and M. Rajabi, *Microchim. Acta*, 2017, **184**, 3027–3035.
- 52 A. Ahmed, A. Hayat, M. H. Nawaz, P. John and M. Nasir, *J. Colloid Interface Sci.*, 2020, **558**, 230–241.
- 53 A. Ahmed, A. Hayat, P. John, M. H. Nawaz and M. Nasir, *J. Nanostruct. Chem.*, 2021, **11**, 675–691.
- 54 H.-T. Ren, S.-Y. Jia, Y. Wu, S.-H. Wu, T.-H. Zhang and X. Han, *Ind. Eng. Chem. Res.*, 2014, **53**, 17645–17653.
- 55 S. Vignesh, P. Eniya, M. Srinivasan, J. Kalyana Sundar, H. Li, S. Jayavel, M. Pandiaraman, M. A. Manthrammel, M. Shkir and B. Palanivel, *J. Environ. Chem. Eng.*, 2021, **9**, 105996.
- 56 L. D. Chakkarapani, Z. Bytešniková, L. Richtera and M. Brandl, *Appl. Mater. Today*, 2024, **37**, 102113.
- 57 S. I. Khan, A. Hassan, R. Bano, M. A. Gilani, J. L. Marty, H. Zhang and A. Hayat, *Talanta*, 2024, **267**, 125233.
- 58 W. Wei, S. Zhou, D. D. Ma, Q. Li, M. Ran, X. Li, X. T. Wu and Q. L. Zhu, *Adv. Funct. Mater.*, 2023, **33**, 2302917.
- 59 A. Hayat, L. Barthelmebs and J.-L. Marty, *Sens. Actuators, B*, 2012, **171–172**, 810–815.